Shchepanovska, D., Shannon, R. J., Curchod, B., & Glowacki, D. R. (2021). Nonadiabatic kinetics in the intermediate coupling regime: comparing molecular dynamics to an energy grained master equation. *Journal of Physical Chemistry A*, *125*(16), 3473-3488. https://doi.org/10.1021/acs.jpca.1c01260

Nonadiabatic Kinetics in the Intermediate Coupling Regime: Comparing Molecular Dynamics to an Energy Grained Master Equation

Darya Shchepanovska[1], Robin J. Shannon[1], Basile F. E. Curchod[2,*], and David R. Glowacki[1,3,4,*]

[1]School of Chemistry, University of Bristol, Bristol, BS8 1TS, UK; [2]Department of Chemistry, Durham University, Durham, DH1 3LE, UK; [3]Intangible Realities Laboratory, University of Bristol, BS8 1UB, UK; [4]Department of Computer Science, University of Bristol, BS8 1UB, UK

*glowacki@bristol.ac.uk; basile.f.curchod@durham.ac.uk

Abstract

We propose and test an extension of the energy grained master equation (EGME) for treating nonadiabatic (NA) hopping between different potential energy surfaces, which enables us to model the competition between stepwise collisional relaxation and kinetic processes which transfer population between different electronic states of the same spin symmetry. By incorporating Zhu-Nakamura theory into the EGME, we are able to treat nonadiabatic passages beyond the simple Landau-Zener approximation, along with corresponding treatments of zero-point energy and tunnelling probability. To evaluate the performance of this NA-EGME approach, we carried out detailed studies of the UV photodynamics of the volatile organic compound C_6-hydroperoxyaldehyde (C_6-HPALD) using on-the-fly *ab initio* molecular dynamics and trajectory surface hopping. For this multi-chromophore molecule, we show that the EGME is able to capture important aspects of the dynamics, including kinetic timescales, and diabatic trapping. Such an approach provides a promising and efficient strategy for treating the long-time dynamics of photoexcited molecules in regimes which are difficult to capture using atomistic on-the-fly molecular dynamics.

1. Introduction

Accuracy of molecular photodynamic simulations in the excited state is inherently constrained by the dimensionality of the system. Exact non-relativistic quantum mechanical dynamics of a nuclear wavepacket can be described by solving the time-dependent Schrödinger equation, but exponential scaling limits this approach to small molecular systems. At the opposite end of the scale, there is a growing interest in describing the nonadiabatic dynamics of very large systems characterised by exciton transfer between chromophores.[1-5] In fact, an analytical description of nonadiabatic transitions for a simple one-dimensional two-state system in the weak coupling limit has been available since 1932, developed simultaneously, and separately, by Landau, Zener, and Stueckelberg.[6-8] In many cases Landau-Zener (LZ) theory works reasonably well even for larger, multidimensional systems. Later, Zhu and Nakamura built on this framework to produce a set of exact nonadiabatic transition probabilities for different types of nonadiabatic curve crossings.[9-15] Zhu-Nakamura (ZN) theory is valid over the entire coupling regime, is fully analytical, and incorporates tunnelling contributions. Like LZ theory, it is formulated in a single dimension.

On-the-fly trajectory-based semiclassical dynamics accounts for the full dimensionality of a molecular system. For example, Tully's fewest switches surface hopping (FSSH) is a well-known and efficient way of simulating femtosecond timescale processes in the excited state,[16] where the time evolution of a nuclear wavepacket is approximated by a swarm of independent trajectories that classically propagate the nuclear degrees of freedom on a potential energy surface (PES) calculated on-the-fly. Each trajectory can stochastically switch between electronic states in regions of strong nonadiabatic coupling. While FSSH has known shortcomings (including overcoherence, and neglect of tunnelling and interference effects)[17], it often provides an accurate and scalable method that is now widely used to explore photochemical and photophysical phenomena, also for atmospheric chemistry.[18-21] Given that FSSH typically has a sub-femtosecond integration time step, pushing the simulation into the nanosecond regime necessitates compromises with respect to the electronic structure method and number of trajectories. It has been suggested that this bottleneck might be overcome through machine learned energies and couplings.[22]

For longer timescale simulations in the statistical regime, alternatives to conventional nonadiabatic dynamics strategies are needed. The energy grained master equation (EGME) is the numerical implementation of the exact master equation which discretises the density of states ρ, recasting it in matrix form. The EGME has recently been applied to the study of non-RRKM reaction kinetics in the gas phase,[23] in solution,[24, 25] and in surface chemistry.[26] Unlike FSSH, where an electronic structure calculation is performed at each step of a trajectory, an EGME calculation needs only the energies, frequencies and rotational constants of the relevant stationary points. This allows for the use of more computationally demanding electronic structure calculations and detailed sensitivity analyses on the results. The EGME also enables treatment of collisional activation and energy dissipation from the system. Furthermore, unlike molecular dynamics simulations where zero-point energy can leak, vibrational zero-point energy at the stationary points can be included explicitly in an ME calculation. Approaches to zero-point energy conservation in quantum-classical trajectories exist,[27] but they are not adopted in the standard FSSH algorithm used in this work. Tunnelling corrections may also be included in the framework of the EGME approach using an asymmetric Eckart barrier[28] or semiclassical WKB theory.[29] Solving the ME returns temperature and pressure dependent species profiles, making it a useful tool for modelling atmospheric or interstellar reactions.

Nonadiabatic analogues of standard statistical rate theories generalise classical transition state theory (TST) to reactions involving multiple PESs.[30-32] For example, intersystem crossings have been successfully modelled by using both the LZ and ZN expression for the inter-state surface hopping probability at the minimum energy crossing point (MECP).[33-36] Until recently, simulation of intersystem crossings in the surface hopping framework has been limited by the need for the global calculation of the spin-orbit coupling matrix elements[37] or spin-orbit coupling gradients.[38] It is now possible to run FSSH simulations that include coupling between states of arbitrary spin multiplicity.[39, 40] Using the LZ approach to describe coupling between states with differing multiplicity works well in the weak coupling regime, but fails for strong coupling.[6] A nonadiabatic EGME model (NA-EGME) of internal conversion should instead use the ZN expression, which is able to accurately treat the analytical nonadiabatic transition probabilities for the full range of energies and couplings,[10] giving the LZ result in the weak coupling limit, and the transition state theory result in the strong coupling limit. The ZN description of the coupling region can also be formulated to include contributions from tunnelling through the crossing barrier. In contrast to the full-DOF description of quantum-classical dynamics, the ZN equations are only formulated for 1-D crossings. Here, we provide

evidence that – for seam-like crossings – the ZN approach offers a good approximation to describing nonadiabatic transitions between adiabatic states.

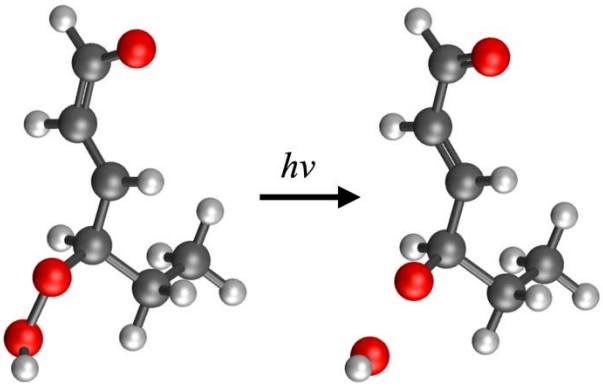

Fig. 1: Main reaction channel for C_6-HPALD photodissociation in 300-400 nm range.[41]

In this work, we apply the NA-EGME to predict the dissociation rate of a photoexcited bi-chromophoric hydroperoxy aldehyde, C_6-HPALD, whose primary photodissociation channel is shown in Fig. 1. In order to evaluate the validity of this approach, we show that the NA-EGME results are similar to the outcomes of nonadiabatic molecular dynamics (NA-MD, in this case FSSH). HPALDs are a class of molecules important in atmospheric chemistry, and it has been suggested that they participate in OH radical recycling in low NO_x regions of the troposphere.[42-47] As a product of isoprene oxidation, they contain an α,β-enone chromophore that absorbs sunlight in the UV range, which is close to a labile peroxide bond. Previous experiments investigating the photodissociation kinetics of C_6-HPALD reported OH radical production under UV light.[41] In this paper, we are less concerned with the atmospheric details of HPALD photodissociation, but rather with C_6-HPALD as a prototypical example of a multi-chromophore system with an interesting seam-like nonadiabatic coupling topology between two low-lying excited states. We show that the dissociation rate obtained using a NA-EGME model shows qualitative agreement with the results of NA-MD, at a significantly reduced computational cost.

This paper is structured as follows. First, we describe how nonadiabatic effects can be included in an EGME model using ZN transition probabilities. Second, we describe the electronic structure calculations used to characterise the relevant excited states of C_6-HPALD in the Franck-Condon region, and along the dissociative coordinate. Third, we describe the NA-MD and NA-EGME calculations and their adiabatic counterparts. Fourth, we compare the results of these contrasting methods for a single isolated reaction coordinate which corresponds to the molecule moving over a transition state on the S_1 surface leading to photodissociation. Lastly, we extend both models to include all rotational conformers of C_6-HPALD.

2. Methods

2.1 Constructing a nonadiabatic master equation

The energy grained master equation (EGME) is a Markov-state model that has found widespread application to non-equilibrium problems in chemical kinetics.[24, 25, 48-50] Most applications of EGME models focus on reactive processes on a single electronic state and do not incorporate nonadiabatic coupling. While strategies for calculating microcanonical rate coefficients for nonadiabatic processes do exist, to our knowledge there has only been one attempt to incorporate such transitions into an EGME framework. Plane *et al.*[49] modelled temperature and pressure dependent intersystem crossing kinetics by treating the extended

seam between the singlet and triplet state as a dividing surface. The MECP between the states was treated as a pseudo-transition state, and the probability of spin-forbidden hopping transitions between these states was calculated by convoluting the density of states at the MECP with the LZ expressions to obtain microcanonical rate coefficients.

Building on the work of Plane *et al.*, we have extended the NA-EGME to calculate the rate of HPALD photodissociation, where the nonadiabatic transition of interest involves coupling between two states of the same multiplicity – i.e., significantly stronger coupling than the intersystem crossing investigated by Plane *et al.* The LZ model is ill-suited to internal conversion as it assumes the inter-state coupling is localised, and weak. For these reasons, we used ZN theory to describe nonadiabatic transition probabilities in the coupling region. The ZN equations produce the correct analytical hopping probability coefficients over the full range of coupling regimes for a 1-D nonadiabatic tunnelling type crossing,[10, 51] returning the LZ result in the limit of weak coupling, and the classical transition state theory result in the limit of strong coupling.

An adiabatic master equation model (A-EGME, illustrated in Fig. 2) is constructed from any number of connected potential energy wells (isomers) and the transition states between them. In order to make the problem computationally tractable, the energy of each species is discretised into bins or grains of a set size. The population density across each energy grain of every isomer in the system is then defined by a vector $\mathbf{n}(E,t)$, and it is possible to formulate a set of coupled differential equations in terms of $\mathbf{n}(E,t)$ that describe the time-evolution of the grain populations. Recasting these differential equations in matrix form defines the chemical master equation.

$$\frac{\partial \mathbf{n}(E,t)}{\partial t} = \mathbf{M}\mathbf{n}(E,t) \tag{1}$$

The matrix **M** is expressed as [ω(**P-I**)-k], where ω is the Lennard Jones collision frequency, **P** is a matrix of transition probabilities between grains, **I** is the identity, and k is a diagonal matrix of energy-resolved microcanonical rate constants, $k(E)$, for the reactive process. In the EGME, population transfer between grains can arise due to interactions with a bath gas or through reactive loss/gain to a connected isomer. Energy transfer as a result of bath interactions is typically modelled using an exponential down model. For reactions between different isomers, population transfer can only occur between corresponding grains of the same energy. This is included in the model through unimolecular microcanonical rate coefficients $k(E)$ calculated from Rice-Ramsperger-Kassel-Marcus (RRKM) theory. The RRKM microcanonical rate coefficient at energy E is

$$k(E) = \frac{W(E)}{h\rho(E)} \tag{2}$$

where $W(E)$ is the sum of rovibrational states at the optimised transition state geometry, and $\rho(E)$ is the density of rovibrational states for the isomer.

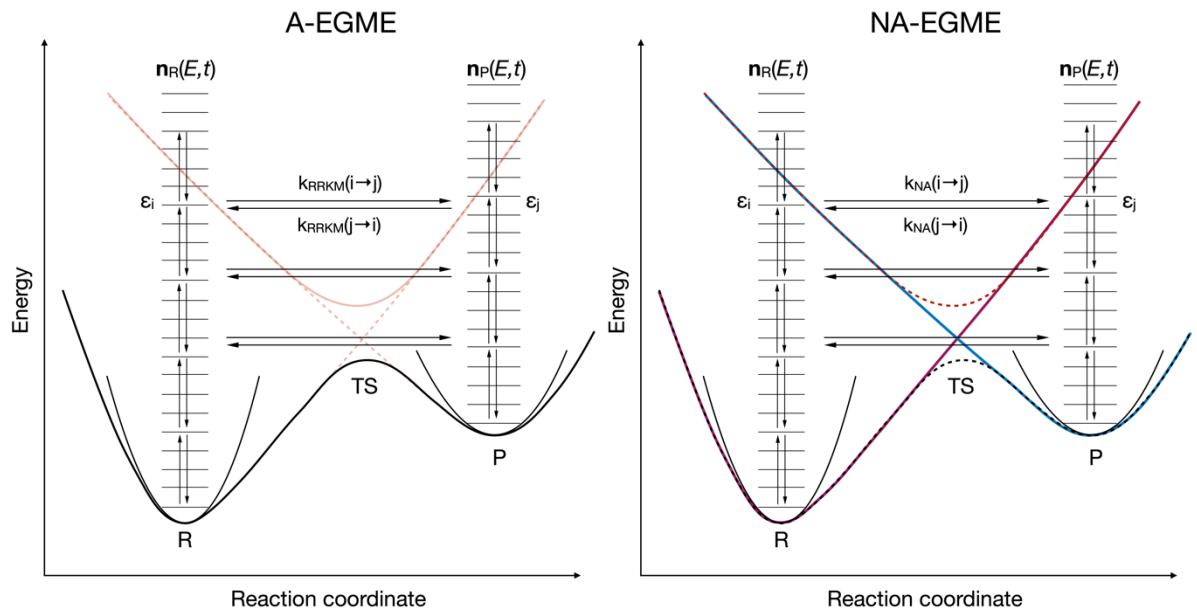

Fig. 2: Left hand panel shows a standard A-EGME model describing a reactant and product species connected by a transition state. Right hand panel shows the NA-EGME, with nonadiabatic transitions integrated through the inclusion of energy resolved ZN transition probabilities to the upper state.

Because the EGME can be used to model out-of-equilibrium phenomena,[52] it is often applied to reactions in atmospheric and combustion chemistry which cannot be modelled with equilibrium TST techniques due to the non-Boltzmann distribution of energy in isomers. This allows us to replicate the non-equilibrium energy distribution of a wavepacket directly following photoexcitation.

The NA-EGME model, illustrated in Fig. 2, is constructed analogously to the conventional ground state A-EGME, except that the microcanonical rate coefficients are not calculated through RRKM theory. Nonadiabatic coupling between states is included through an energy resolved ZN expression for the transition probabilities P_{ZN} between two diabatic states in the vicinity of a crossing point. We can then compute a set of nonadiabatic microcanonical rate coefficients $k_{NA}(E)$ which transfer population between the different diabatic states. The expression for $k_{NA}(E)$ is similar to the RRKM expression in equation 2,

$$k_{NA}(E) = \frac{N_{TS}(E)}{h\rho_{S_1}(E)} \tag{3}$$

where the density of states at the optimised S_1 minimum is ρ_{S_1} and N_{TS} is the convolution of the ZN transition probabilities P_{ZN} and density of states at the transition state ρ_{TS}.

$$N_{TS}(E) = \int_0^{E'} \rho_{TS}(E - E')P_{ZN}(E)dE' \tag{4}$$

The complete equations for P_{ZN} are available in the SI, and implemented in MESMER (master equation solver for multi-well energy reactions).[53]

3. Computational details

3.1 Characterising the excited state PESs

C_6-HPALD is a conformationally flexible molecule. A systemic rotor search performed in Avogadro V1.2.0 finds 7 conformational isomers which we label A-G. Ground state geometries of these conformers were then optimised with DFT/PBE0/TZVP and their analytical frequencies confirm that these geometries are local minima on the ground state PES.

Excited state properties, including energies, nuclear gradients, and nonadiabatic couplings, can be calculated accurately and efficiently with linear response time dependent density functional theory (LR-TDDFT). LR-TDDFT, like DFT, is formally exact on the condition that the true frequency-dependent exchange correlation functional is used. Its shortfalls are well documented, including its tendency to underestimate energies of states with high charge transfer character[54] or regions of the PES with strong coupling between ground and excited states.[55] Nevertheless, LR-TDDFT is widely used for nonadiabatic dynamics simulations of larger systems due to its favourable scaling with basis set size.[56, 57] Employing LR-TDDFT for excited state dynamics, however, always requires a careful validation of its accuracy in comparison to high-level wavefunction methods.

To determine a method for running NA-MD in the relevant region of the PESs, we performed a number of excited state benchmarks at the S_0 geometry of the lowest energy conformer (B) of C_6-HPALD. A scan along the PES cross section of the -O-OH internal coordinate was initiated at the S_0 geometry of conformer B to validate the use of LR-TDDFT/PBE0/6-31G (calculated for 5 singlets) against MS(4)-CASPT2(10,8)/6-31G* and a number of other methods. The active space of the MS-CASPT2 calculation was selected to include the bonding and anti-bonding orbitals of the peroxide and α,β-enone chromophores, as well as the lone pairs on the oxygen atoms. All DFT/LR-TDDFT calculations in this paper were performed in Gaussian 16.[58] Ground state energies at the optimised geometries were refined with density fitted CCSD(T)-f12//cc-pVDZ-f12//def2-QZVPP in Molpro 2019.[59] MS-CASPT2 calculations were performed in OpenMolcas v18.09.[60]

The transition state (S_1-TS) on the S_1 surface was optimised using an eigenvector following Berny algorithm in Gaussian 16[58] with LR-TDDFT/PBE0/6-31G. Finding this first order saddle point on the S_1 surface was not a trivial task: because the seam is quite sharp, optimisation steps that were too large would cause it to fall down the steep slopes of the ridge. The S_1-TS geometry was verified through a vibrational frequency analysis that yielded a single imaginary frequency. An intrinsic reaction coordinate (IRC) scan was performed, initiated at this S_1-TS geometry. Geometries of each conformer were optimised in the S_1 state with the optimisation starting at their respective S_0 geometry. The minimum energy conical intersection (MECI) between the S_1 and S_2 states was optimised by using the search algorithm described by Harvey *et al.*.[61]

3.2 Predicting the photoabsorption cross section to calculate photolysis rate

The photoabsorption cross section of C_6-HPALD has yet to be measured experimentally. We can predict it with *ab initio* methods by using the nuclear ensemble approach based on a harmonic Wigner distribution in the ground state[62] which captures the broadening of the spectral bands. Ground state frequencies used to generate the Wigner distribution were calculated for each conformer with DFT/PBE0/TZVP. For each of the 7 conformers, 100 nuclear configurations are sampled from their respective distribution. We calculate the absorption in the 300-400 nm range into the S_1 and S_2 electronic states separately, as well as the combined spectrum. For each sample point the vertical transitions and oscillator strengths are calculated with LR-TDDFT/PBE0/TZVP. Each peak is overlaid with a Lorentzian curve

whose phenomenological broadening is set to 0.05 eV to return a continuous spectrum. The final photoabsorption cross section is a linear combination of the spectra for each conformer where the Boltzmann weights of the conformers ω_{conf} are calculated from their CCSD(T) electronic energies. We approximated the Gibbs free energy by the electronic energy because free energy corrections (from PBE0/TZVP frequencies) did not change the ordering of states.

3.3 Trajectory surface hopping dynamics

All trajectory dynamics simulations were performed using the following protocol, unless stated otherwise. Fewest switches surface hopping simulations were performed in Newton-X.[31, 63] Energies and gradients of the first four singlet states (S_0- S_3) were calculated at each step with LR-TDDFT/PBE0/6-31G using Gaussian 09.[64] Energy based decoherence corrections were applied, as described by Granucci and Persico,[65] with the decoherence parameter α set to 0.1 a.u. Nonadiabatic coupling terms between electronic states were calculated using a time-derivative coupling scheme.[66]

The importance of the nonadiabatic effects was quantified by comparing against adiabatic molecular dynamics (A-MD) in which the nonadiabatic coupling between states was set to 0, effectively restricting the trajectories to the S_1 state. A-MD calculations were also performed in Newton-X with identical initial conditions to the NA-MD run.

Starting geometries and velocities for the trajectories were generated by randomly sampling points from a ground state Wigner distribution (for harmonic oscillators). For each conformer this distribution was constructed using DFT/PBE0/TZVP level normal mode frequencies at the optimised S_0 geometries, where a larger basis set is selected to improve the quality of the distribution. In total, we ran 250 NA-MD and 50 A-MD trajectories, whose initial conditions corresponded to the Wigner distribution of conformer C. A further 109 trajectories were performed with both NA-MD and A-MD, corresponding to the realistic conformer distribution where the number of trajectories corresponds to the Boltzmann weight of the conformer in the ground state. All trajectories were initiated on the S_1 electronic state as it corresponded to the strongest peak in the actinic region, $\lambda > 320$ nm, of the photoabsorption cross section (available in the SI, S5).

All trajectories were propagated up to 4 ps or until photodissociation was observed. Total energy was conserved in all trajectories up to the end point of the trajectory. Because LR-TDDFT fails to describe homolytic bond dissociation, trajectories were stopped soon after the dissociation was initiated. Classical nuclei were propagated with a 0.5 fs time step. The rationale behind this choice is discussed further in the SI (S9).

3.4 Constructing a nonadiabatic EGME model from stationary points on the excited state PES

Each electronic structure calculation used to construct an EGME model was performed at the same level of theory (LR-TDDFT/PBE0/6-31G) as that used for NA-MD so that we might directly compare the results. Energies of all stationary points were specified with respect to the energy of the geometry optimised S_1 minimum which was treated as the reactant well in the model. Zero-point energy corrections were not used when defining the relative energies so as to make a direct comparison with results of dynamics calculations, in which ZPE was not rigorously constrained.

The electronic structure theory codes which we utilized provided states energies in the adiabatic (S_0, S_1, S_2, etc.) representation. However, as illustrated in Fig. 2, the NA-EGME treats the different states in the diabatic representation (in this case an $n\pi^*$ and $n'\sigma^*$ state), and requires as input an analytical form of the diabatic states in the vicinity of the crossing point to determine P_{ZN} at the seam. To derive a diabatic representation from the adiabatic energies, we considered only the coordinate along the imaginary eigenvector of the S_1-TS Hessian, investigating 1D motion along the 3N-7 dimensional coupling seam. The eigenvector describing this motion takes the system across the $n\pi^*/n'\sigma^*$ seam, which corresponds to extension of the peroxide bond and loss of OH, denoted by reaction coordinate R. Energies of the S_1 and S_2 adiabatic states across this coordinate are used to fit the diabatic states near the TS. We do this by constructing a simple Hamiltonian, $\mathbf{H}(R)$, which includes the two diabatic states and a coupling between them (H_{12}), assumed to be constant in that region.

$$\mathbf{H}(R) = \begin{pmatrix} H_{11}(R) & H_{12} \\ H_{12} & H_{22}(R) \end{pmatrix} \tag{6}$$

Analytical expressions for its two eigenvalues, λ_1 and λ_2 are determined by diagonalizing $\mathbf{H}(R)$. These eigenvalues correspond to the S_1 and S_2 adiabatic states respectively. Calculated adiabatic states were fitted to the analytical forms of the diabats given in equation 7. We assumed the dissociative state $H_{22}(R)$ to have the form of an exponential decay, and the bound state, $H_{11}(R)$, to have the form of a harmonic well.

$$\begin{aligned} H_{11}(R) &= A_{\pi*}(R - \beta_{\pi*})^2 + \varepsilon_{\pi*} \\ H_{22}(R) &= A_{\sigma*} exp(-R\beta_{\sigma*}) + \varepsilon_{\sigma*} \end{aligned} \tag{7}$$

The fitted parameters (S11, S12) were used in the NA-EGME calculation to determine P_{ZN} and calculate a set of microcanonical rate constants for each energy grain.

The initial population vector $\mathbf{n}(E,t_0)$ was set up with N energy grains. To replicate the energy distribution of the wavepacket at the start of the dynamics, $\mathbf{n}(E,t_0)$ must mirror the initial conditions used in the NA-MD calculations. Each initial condition sampled from the Wigner ensemble corresponds to an initial energy, a sum of its kinetic energy and its potential energy referenced to S_1. The distribution of total energies resembles a normal distribution, with an average initial energy above the S_1 minimum. This average energy corresponds to the n_i^{th} energy grain in the population vector $\mathbf{n}(E,t)$ so the EGME calculations are initiated with 100% of the initial population in this grain.

We used a grain size of 50 cm^{-1} in all EGME calculations and standard temperature and pressure (300K and 760 Torr) to replicate atmospheric conditions. Collision parameters used for the bath gas, He, were ε = 10.2 K and σ = 2.55 Å and the collisional energy transfer was treated using an exponential down model.[67] The collisional energy transfer parameter is set to 250 cm^{-1}, a value which is typical under standard atmospheric conditions.[50] Photodissociation was assumed to be irreversible and the dissociation products were treated as a sink. To quantify the impact of nonadiabatic effects at the $n\pi^*/n'\sigma^*$ seam in these EGME calculations, the same model was re-run without allowing nonadiabatic transitions, using a standard non-equilibrium ground state EGME model. Microcanonical $k(E)$ were calculated using RRKM theory.

The NA-EGME model was then modified by substituting MS(4)-CASPT2/6-31G* energies at the same LR-TDDFT optimised stationary points to refine the EGME result. These calculations use the same frequencies and rotational constants calculated with LR-TDDFT/PBE0/6-31G.

Single point energy calculations were performed for the following geometries: the S_1 minimum of the B conformer; geometries found by taking steps along the imaginary eigenvector of S_1-TS. For the latter case, a crossing point between the diabatic surfaces is found at a small displacement from the S_1-TS geometry. New diabats were fitted to the results of the scan, leading to slightly different ZN parameters.

All EGME calculations reported in this study were performed using the open source master equation solver, MESMER.[53]

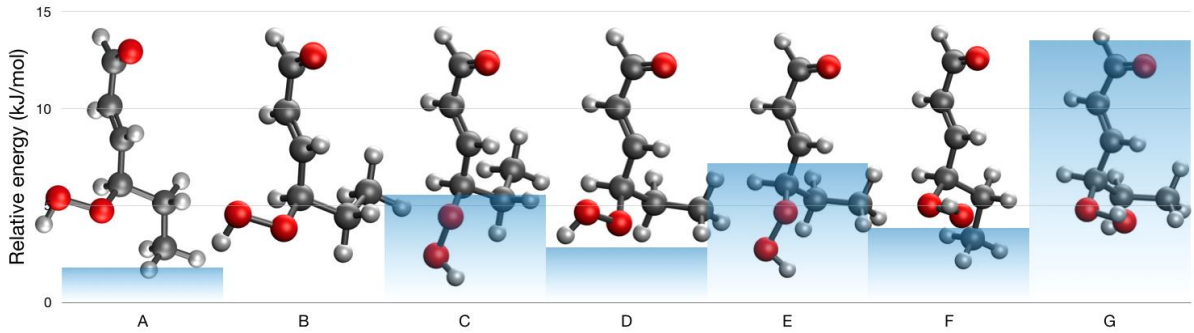

Fig. 3: Geometries of the 7 rotational isomers of C_6-HPALD. Relative energies, shown on chart, are refined with df-CCSD(T)-f12//cc-pVDZ-f12//def2-QZVPP.

4. Results and Discussion

4.1 Characterising the S_1 and S_2 PESs in the Franck-Condon region and at the crossing seam

Ground state geometries and relative CCSD(T) energies of all 7 conformers are shown in Fig. 3. Optimising these rotamer structures on the S_1 PES with LR-TDDFT converged on 7 distinct structures that maintain the orientation of the peroxide and ($-CH_2CH_3$) branches such that there are multiple S_1 minima. Conformer B remained the lowest energy conformer on the S_1 PES.

Our predicted photoabsorption cross section $\sigma(\lambda)$, available in the SI, indicated that the majority of the photoexcitation in the UV-Vis region is into the S_1 state. Integrating over $\sigma(\lambda)$, actinic flux, and quantum yield in the actinic region we can make an *ab initio* estimate of the photolysis rate. Assuming a unity quantum yield we predict it to be 1.4×10^{-4} s^{-1}, within a factor of three of the observed experimental rate of $6.3\pm0.1\times10^{-5}$ s^{-1}.[41] The cross-section indicates that in the actinic region the strongest peak corresponds to absorption into the S_1 state.

Shapes of the excited state PESs along the peroxide bond coordinate calculated with LR-TDDFT/PBE0/6-31G and MS-CASPT2(10,8)/6-31G* show good qualitative agreement. On this basis, we decided to use LR-TDDFT/PBE0/6-31G as the electronic structure method for all NA-MD and A-MD calculations in this paper. Rigid scans along the peroxide bond dissociation coordinate in Fig. 4 show a near degenerate region between the S_1 and S_2 states at 1.65 Å, and between S_2 and S_3 states at 1.76 Å. Benchmarks using larger basis sets show that as the bond extends beyond 1.75 Å, LR-TDDFT provides a poor description of homolytic dissociation. This, however, will not be a significant problem for the dynamics because the S_1 potential is dissociative beyond this point, at which point trajectories were terminated.

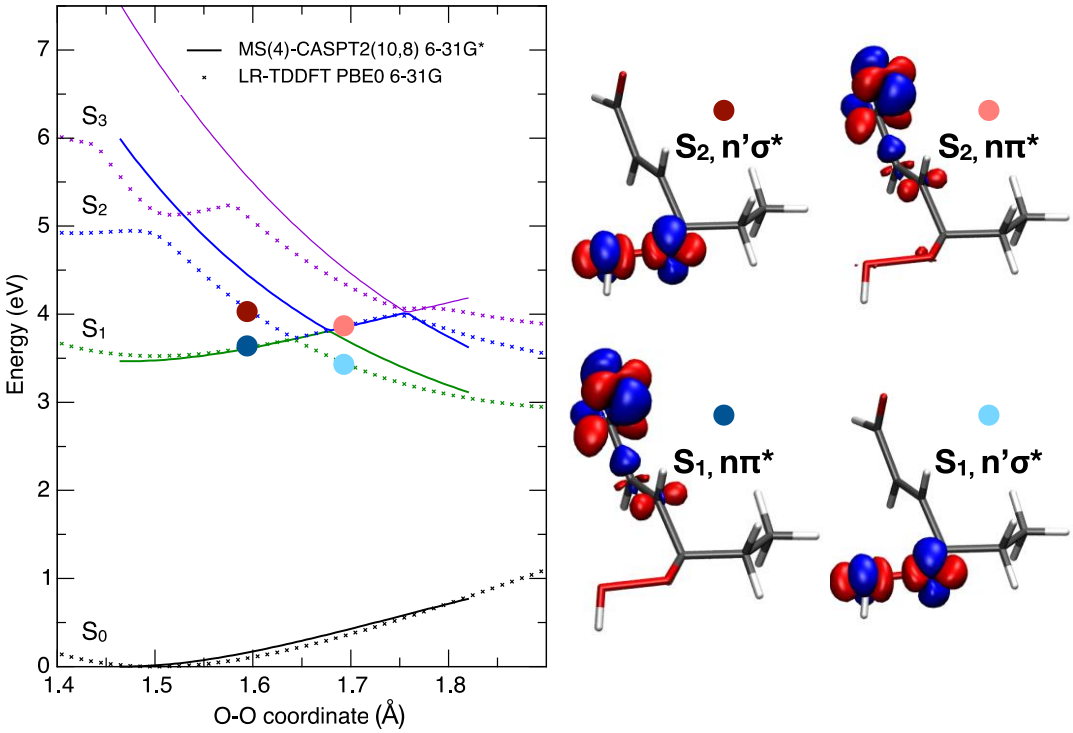

Fig. 4: Energies of the first 4 excited states of conformer B calculated with LR-TDDFT/PBE0/6-31G and MS(4)-CASPT2(10,8)/6-31G*, alongside electron density difference plots between S_0 and specified state at 2 points along the peroxide bond coordinate illustrating the change in diabatic character.

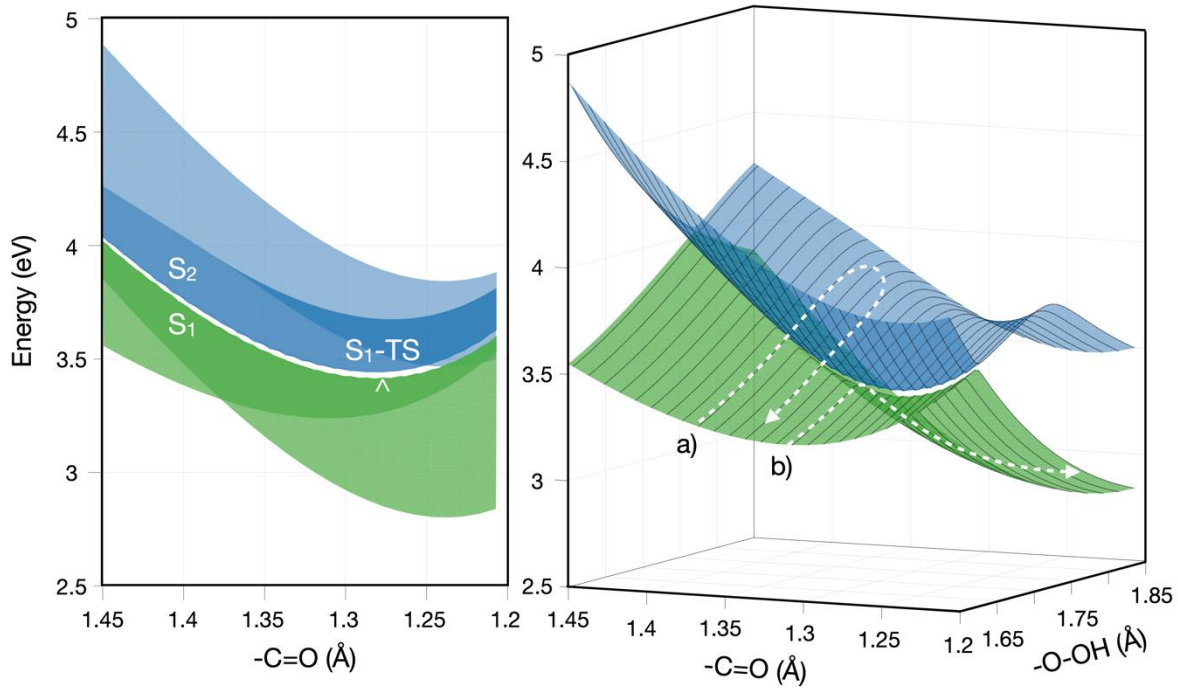

Fig. 5: Scan of the S_1/S_2 nonadiabatic seam initiated at S_1-TS, excitation energies calculated with LR-TDDFT/PBE0/6-31G. Left panel highlights the extended near-degenerate (3N-7) seam. a) Diabatic trapping mechanism; b) Adiabatic passage across seam leading to loss of OH.

The density difference plots shown in Fig. 4 shows that the $n\pi^*$ transition which characterises the S_1 state in the bound region of the PES (O-O extended to 1.6 Å) is located mostly on the

α,β-enone chromophore. At the same geometry, the n'σ* transition to the S_2 state is located mostly along the -O-OH bond. When the peroxide bond is extended to 1.7 Å, the electronic character of the two states swaps, such that the S_1 state is now characterised by the n'σ* transition. The region of strong nonadiabatic coupling observed between the S_1 and S_2 at 1.65 Å in Fig. 4 is a single point on an extended (3N-7) seam where the nπ* and n'σ* diabatic states cross. We located critical points along this seam which included an S_1/S_2 MECI as well as a saddle point on the S_1 surface (S_1-TS) which is the minimum energy geometry in the space of this seam. The energy of the MECI is 31.3 kJ mol^{-1} above the S_1 minimum of the lowest energy conformer, B. The energy of the S_1-TS is at 16.1 kJ mol^{-1} relative to conformer B. Visualising the normal mode corresponding to the only imaginary frequency at the S_1-TS showed synchronization between stretching in the -O-OH coordinate and compression in the C=O coordinate. This highlights that this mode couples the α,β-enone and peroxide chromophores and therefore will be important for describing the reaction coordinate. Furthermore, the remarkably high value of the imaginary frequency (ν_{im} = -3534.1 cm^{-1}) illustrates the sharpness of the (3N-7) seam in the vicinity of the S_1-TS. To visualise this seam, we performed a rigid 2D scan along the -C=O and -O-OH stretching coordinates of C_6-HPALD that correspond to the two coupling chromophores. Results of this scan are shown in FFig. 5.

An intrinsic reaction coordinate (IRC) scan initiated at the S_1-TS geometry converges on the dissociated structure and the S_1 minimum of conformer C, as can be seen in Fig. 6. Energies, frequencies, and rotational constants at these critical points are tabulated in the SI.

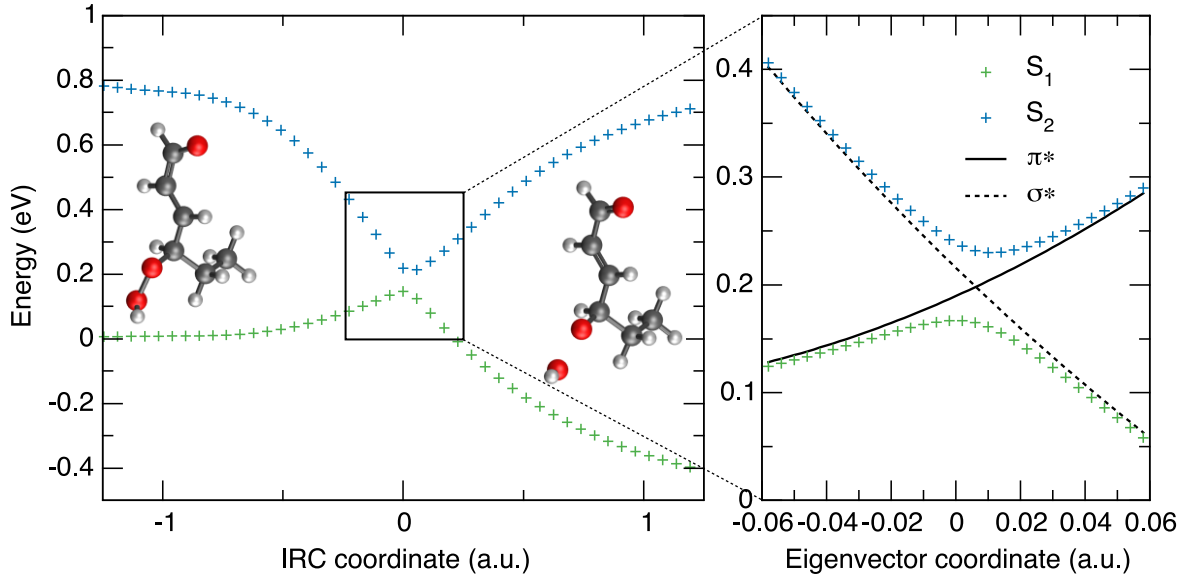

Fig. 6: Intrinsic reaction coordinate scan started at the S_1-TS. Energy is shown relative to the S_1 minimum of conformer C. Geometries are shown at the terminal step of the IRC scan. Right panel shows a scan across the TS geometry along the eigenvector of the imaginary normal mode. Fitted diabatic states used in the NA-EGME calculation are shown in black.

4.2 Direct comparison between NA-EGME and NA-MD for a single conformer

Our exploration of the excited state PES located a direct reaction coordinate between the S_1 minimum of conformer C and the S_1-TS, shown by the IRC in Fig. 6. In the following section,

we consider a simple photodissociation model based on a potential well (S_1-C) and a single barrier (S_1-TS) linked by this reaction coordinate, that ignores all other C_6-HPALD conformations. We should highlight that the dissociation rate calculated here is distinct from the photolysis rate calculated in section 4.1; it is difficult to obtain a direct experimental measurement of the dissociation rate, given that experimental studies involve a photoexcitation step (and corresponding photo-excitation rate) which prepares the molecule in S_1.

4.2.1 Description of the seam crossing and OH loss rate from NA-MD

We began by running 50 A-MD and NA-MD trajectories, whose initial conditions were sampled from the ground state Wigner distribution of conformer C. The two sets of trajectories shown in Fig. 7 are projected on to the -C=O and -O-OH coordinates, illustrating the passage of trajectories across the seam. By observing HPALD dynamics prior to dissociation we see that the molecule remains in the S_1 potential well for a number of vibrational periods and explores the available phase space within its initial conformation.

For all 50 NA-MD trajectories the net adiabatic population remained largely on the S_1 state, with 90% hopping to the S_2 state at some point during the run. Only a single trajectory hopped to the S_3 state, and no population on S_0 was ever observed. On this timescale we expect that the dynamics are limited to the S_1 and S_2 adiabatic states. In the Franck-Condon region of the PES the S_1 state exhibits $n\pi^*$ character and is near an S_1 PES minimum. A-MD trajectories in Fig. 7 indicate that for loss of OH to occur, the -O-OH coordinate must extend in concert with the compression of the -C=O bond, causing the S_1 state to change character from predominantly $n\pi^*$ to the dissociative $n'\sigma^*$ character. The nuclear wavepacket must necessarily proceed across the seam adiabatically, however hopping to the non-dissociative S_2 state can occur.

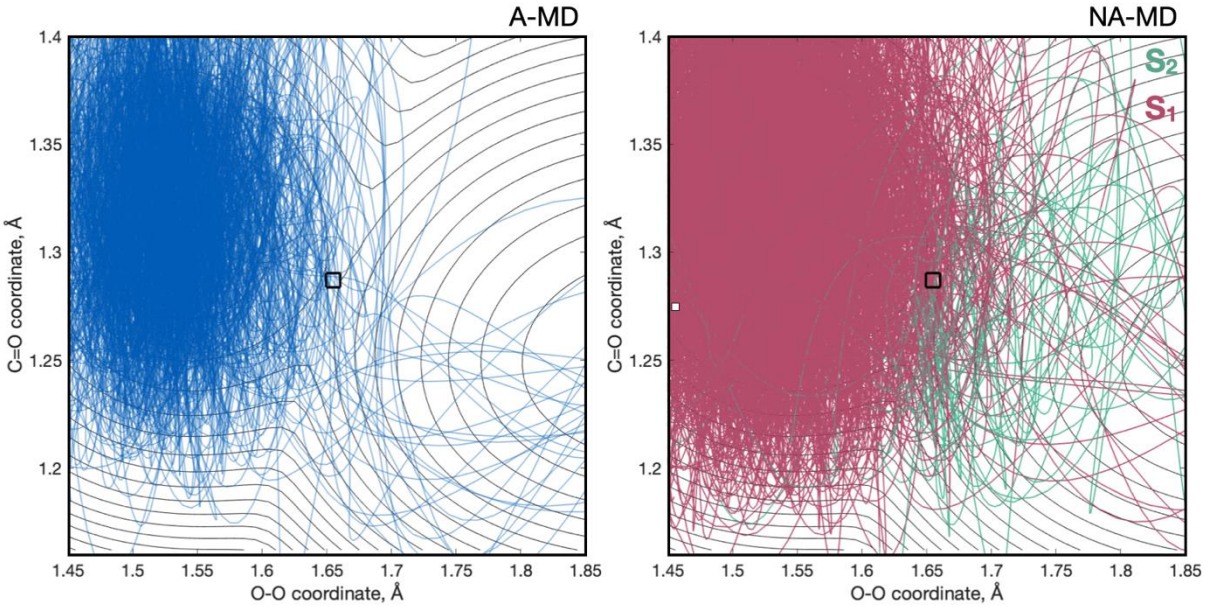

Fig. 7: Projection of 50 A-MD and NA-MD trajectories of conformer C into the -C=O and -O-OH coordinates. NA-MD panel (right) illustrates the switch from S_1 to S_2 with a colour change. Background contour plot shows the shape of the S_1 PES from a rigid scan initiated at the S_1-TS (indicated by the black square) then scanned across these two coordinates, illustrating the S_1 potential energy well where the trajectories are initialised, and the dissociative potential on the other side of the barrier.

In Fig. 7, we observe that while many NA-MD trajectories that travel across the barrier rebound back towards the S_1 well, almost all A-MD trajectories which cross the barrier dissociate. In the nonadiabatic case such motion visibly corresponds with a switch to the S_2 state. This

mechanism is referred to as diabatic trapping (originally described by Martínez *et al.* as up-funnelling) whereby a trajectory remains on the same diabatic state as it crosses the coupling region thereby preserving its electronic character.[68, 69] Because of this, OH loss is faster for A-MD trajectories since crossing this (3N-7) seam will necessarily lead to a dissociative outcome, whereas in NA-MD the trajectory might become trapped in S_2 and rebound instead. A similar upwards hopping process is observed in the work of Blancafort *et al.* in the bis-adamantyl radical cation that contains two weakly coupled chromophores.[70] We note some similarities between their system and ours, such as the extended near-degenerate seam between two adiabatic states. Qualitatively, we note that diabatic trapping is likely in systems where the conical intersection (CI) branching space vectors are of significantly different magnitude, as is the case here (CI branching space vectors available in the SI, S8).

Next, we consider the rate of dissociation as determined by the dynamics. Three possible outcomes have been observed in the NA-MD results: loss of OH (38 trajectories), loss of HO_2 (9 trajectories), and no dissociative reaction (3 trajectories). The corresponding A-MD results are as follows: loss of OH (45 trajectories), loss of HO_2 (3 trajectories), and no dissociative reaction (2 trajectories). A dissociative outcome is defined as the extension of either the C-OOH or O-OH bond coordinate beyond 1.75 Å and 1.9 Å respectively. Benchmark scans of the PES along these coordinates have shown a potential barrier at 1.65 Å, beyond which the molecule is unlikely to recombine. Dissociating trajectories terminated soon after this nonadiabatic barrier is crossed due to the unreliability of LR-TDDFT in its description of homolytic dissociation. These trajectories are included in the analysis up to the point of dissociation since we can assume that once the bond has extended beyond the threshold, the rate coefficient for reassociation is very small. Loss of HO_2 is a minor dissociative channel which has been suggested experimentally for other peroxides.[71] Its mechanism in C_6-HPALD appears to be linked with diabatic trapping because all NA-MD trajectories terminating in this way show an S_2 to S_1 hop 20 fs prior to dissociation. Given its low probability, and because it cannot be treated with a kinetic model, the HO_2 loss channel is excluded in the following analyses.

To ensure that the NA-MD result is converged we ran another 200 trajectories by using the same 50 initial conditions but inserting a new random seed for the surface hopping algorithm 4 times.[72] In Fig. 8 we see that the results are well converged with as few as 50 trajectories. Biexponential fits of HPALD population decay are available in the SI. A biexponential least-squares fit indicates that there are two separate decay timescales.[73] The fast decay corresponds to trajectories that dissociated ballistically (OH loss takes less than 200 fs), while others remained in the pre-dissociative S_1 well until the trajectory was able to cross the seam allowing more time for intra-vibrational relaxation to occur. Decay constants for the slow fraction of the decay are 1.87 ps for NA-MD and 1.29 ps for A-MD.

4.2.2 Calculating rate of OH loss using an NA-EGME model

Our NA-EGME model assumes that to describe the primary photodissociation channel leading to the loss of OH we need only to consider the $n\pi^*/n'\sigma^*$ state coupling along a 1-D coordinate over the top of the TS. This necessitated only a normal mode analysis at the S_1 minimum of conformer C (S_1-C) and the S_1-TS barrier which is energetically 14.13 kJ mol^{-1} higher. The optimised MECI is 15.2 kJ mol^{-1} above the S_1-TS. The 3N-7 dimensional geometry of the nonadiabatic seam means the MECI is unlikely to be an important critical point since the molecule does not need to pass through it to reach the S_2 state. For this reason, the MECI's influence on the dissociation rate can be neglected and we choose not to include it in the model. Total energies of the 50 initial conditions are normally distributed with the average initial

energy at 453.4 kJ mol^{-1} above the S_1-C minimum. This energy corresponds to the 758th grain in the population vector **n**(E,t) and so, the EGME calculations were initiated with 100% of the population in this energy grain.

The HPALD decay rates calculated using A-EGME and NA-EGME are presented in Fig. 8, illustrating that the photodissociation rates obtained with the trajectory-based approaches are qualitatively similar to those obtained from EGME models, and more importantly that both strategies capture the effect of diabatic trapping. Including nonadiabatic effects slows down the decay rate approximately 6-fold ($\tau_{NA\text{-}EGME}$ = 2.72 ps) in comparison to the rate calculated when nonadiabaticity is neglected ($\tau_{A\text{-}EGME}$ = 0.45 ps). The decay rate is shown to be robust to the initial energy grain distribution and small variations in frequencies by the sensitivity analyses provided in the SI.

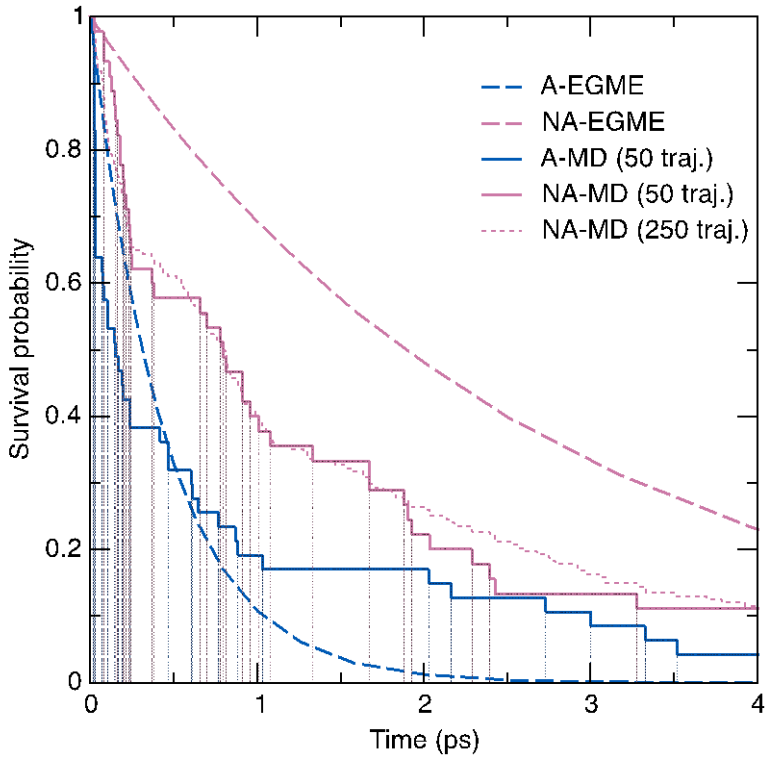

Fig. 8: Comparison of C_6-HPALD decay rate between EGME and trajectory-based methods for conformer C. Convergence of NA-MD at 50 trajectories indicated by the similarity to the 250-trajectory result.

4.3 Comparison of the two extended models, including all conformers

Now that we have shown for the conformer C that both NA-EGME and NA-MD results capture the effect of diabatic trapping during the OH photodissociation process, we will extend this simple model to include all conformers of C6-HPALD highlighted in Fig. 3. For the dynamics calculations we simply projected the ground state conformer distribution into the excited state such that the set of trajectory initial conditions was representative of the rotamer distribution. Boltzmann weights of the A-G conformers (listed in the SI, S2) determine the number of trajectories to be run for each. For TST-type methods like EGME, molecular torsions can be challenging because the rigid rotor approximation breaks down due to the highly anharmonic hindered rotor modes. Ideally, each conformation and its corresponding TS should be treated separately.[74] However, for 7 rotational conformers this approach would necessitate a

cumbersome search for 30 separate TSs in a 3N dimensional phase space. Instead, we propose a pared down model that uses the global conformer minimum (S_1-B) and the S_1-TS to calculate the OH loss rate.

4.3.1 Conformational changes and realistic dynamics of OH loss in NA-MD trajectories

The relative numbers of trajectories initiated at each conformer corresponds to their Boltzmann weight in the ground state calculated using CCSD(T) energies: A: 24; B: 50; C: 5; D: 16; E: 3; and F: 11.

Dihedral angles ϕ_1 and ϕ_2 can be used as a shorthand to distinguish the conformers over the course of a trajectory. This can be seen in Fig. 9 which shows all of the dissociating trajectories exploring the rotational phase space and highlighting that the timescale of conformer interconversion is comparable to that of OH loss. Trajectories corresponding to conformers C and F especially tend to remain conformationally locked, supporting our previous assumption that conformer C could be treated independently. There is a flux of trajectories from conformer B to C suggesting that the rotational barrier towards C is small.

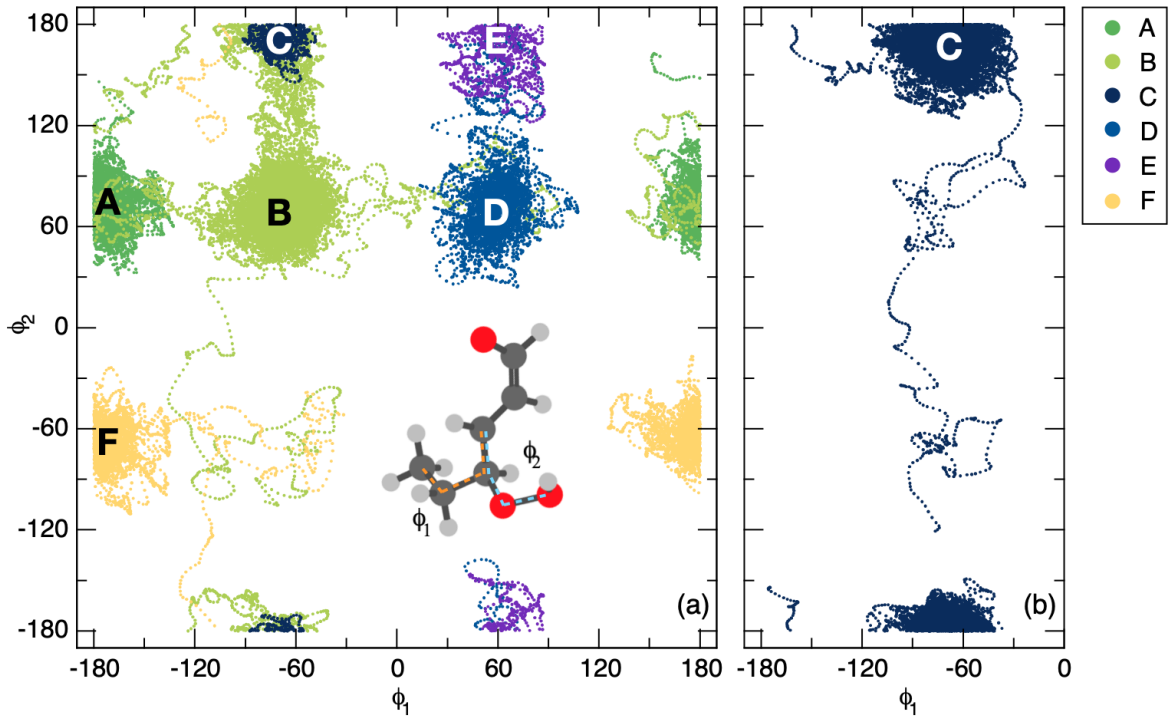

Fig. 9: HPALD conformer interconversion over a 4 ps timescale. Left panel shows the evolution of the two dihedral angle coordinates ϕ_1 and ϕ_2 that define the conformation of the HPALD molecule at a given time step for all 109 NA-MD trajectories. Right panel shows 50 trajectories of conformer C only.

Of the 109 NA-MD trajectories initiated on the S_1 state we observed the following outcomes: loss of OH (50 trajectories), loss of HO_2 (15); no dissociation (43). The corresponding results of the A-MD simulations are: loss of OH (82), loss of HO_2 (10), no dissociation (17). The 95% margin of error shown by the error bars in Fig. 10c illustrates that the difference between dissociative outcomes in adiabatic vs. nonadiabatic simulations is significant.

Analysis of the mean adiabatic population shows that on average population remained on the S_1 surface, rarely falling below 95%, with a fraction of population moving into the S_2 state. Very few trajectories hopped into the S_3 state and no population of the S_0 state was observed on the timescale of the simulation. The survival probability is fitted to an exponential decay, with a first order lifetime, $\tau_{NA\text{-}MD}$, of 4.6 ps. The A-MD results of OH loss are better fitted to a double exponential, shown in Fig. 10d. Approximately a quarter of A-MD trajectories are dissociated on a fast timescale with a lifetime, τ_{fast}, of 58 fs. The rest of the trajectories dissociate on a similar timescale to the NA-MD simulations with lifetime, τ_{slow}, of 2.4 ps.

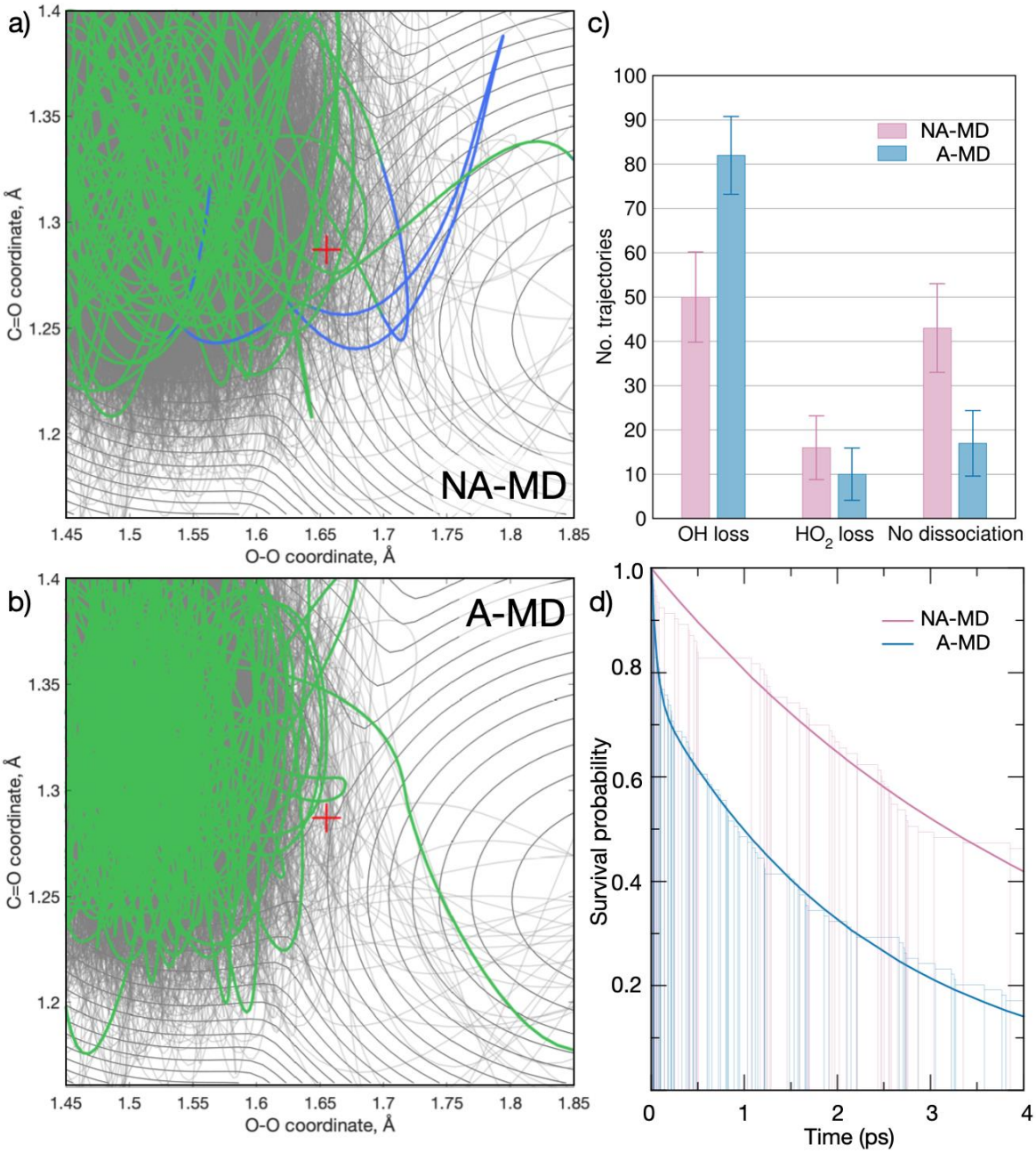

Fig. 10: Dynamics results for all conformers of C_6-HPALD. a) An example of a diabatically trapped trajectory where the switch to S_2 is illustrated by a colour change. b) Example A-MD trajectory that moves in the S_1 well for a number of vibrational periods before crossing the barrier and dissociating immediately. c) Outcomes of the 109 trajectories with 95% confidence intervals showing that differences between NA-MD and A-MD are significant. We calculate the error for a sample proportion

as $Z\sqrt{p(1-p)/n}$ where p is the proportion of trajectories with given outcome, n is the number of trajectories, and Z the multiplier giving the 95% confidence interval. d) Survival probabilities with respect to OH loss, fitted to exponential decay functions.

4.3.2 An approximate all-conformer NA-EGME model for OH loss

Now that we have the results of trajectory dynamics initiated from a realistic ground state conformer distribution, we can construct a new, more realistic, NA-EGME model. Since a large fraction (50 out of 109) of the trajectories were initiated from the conformer B initial condition we use its S_1 minimum as the reactant well (S_1-B) and the S_1-TS. The average initial energy of these trajectories was at 487.0 kJ mol^{-1} above the S_1-B minimum corresponding to the 814th energy grain in the population vector **n**(E,t). Results of the NA-EGME calculations based on this model are shown in Fig. 11. We see that including nonadiabaticity once again has a strong effect on the microcanonical rate coefficients shown in the inset. The nonadiabatic lifetime τ_{ZN} is 1.7 ps, once again ~6x greater than the adiabatic lifetime, τ_{RRKM} = 0.3 ps.

We have tested the importance of torsional anharmonicity using the hindered rotor approach, as implemented in MESMER. This sensitivity analysis ensures that the presence of anharmonic rotational modes does not significantly alter the ratio of densities of states, and the corresponding decay constants. Normal mode frequencies corresponding to torsional motion were projected out of the Hessian.[75] Results of rigid torsional scans performed over 4 torsional bonds at the S_1-B minimum and S_1-TS geometries were input into the MESMER calculation. Results available in the SI (S14) show that incorporating these torsional effects does not significantly impact the reaction profiles. We suggest this could be due to the similarity between torsional profiles at the S_1 minimum and TS geometries that result in a cancellation of errors.

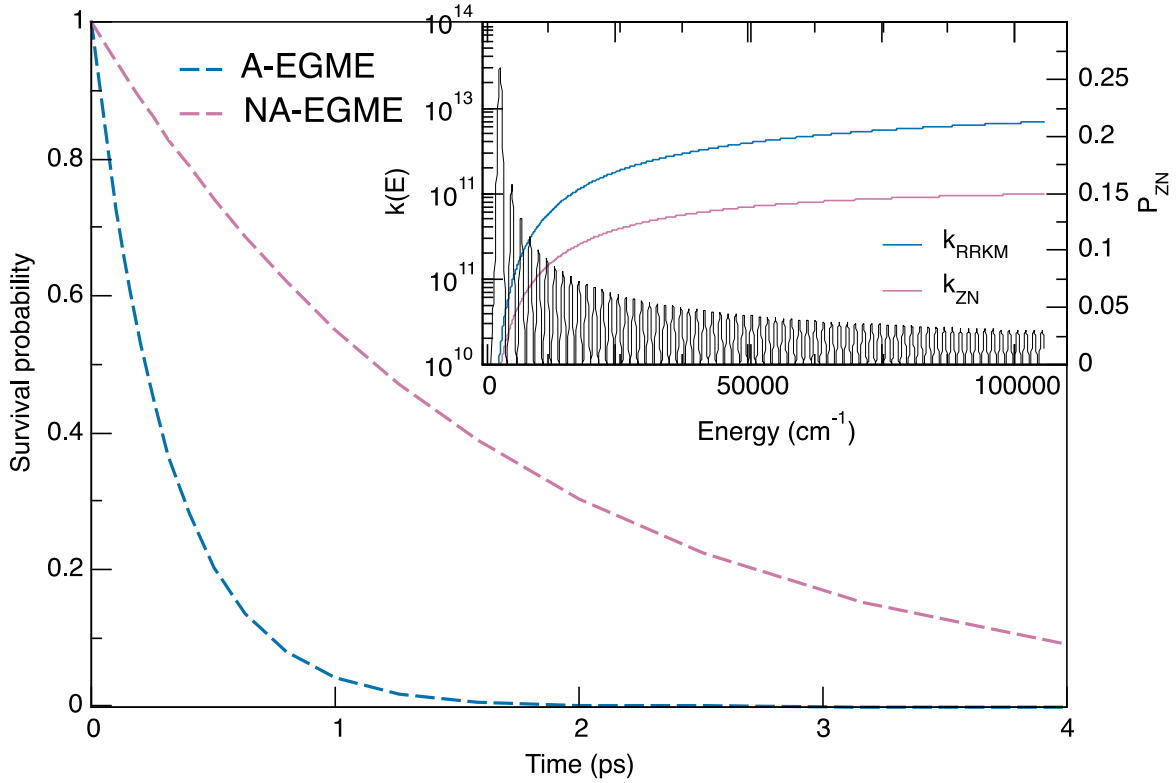

Fig. 11: Results of EGME calculations, with microcanonical rates calculated using an adiabatic (A-EGME) and a nonadiabatic (NA-EGME) expression. Inset shows the energy resolved microcanonical rate constants (k_{RRKM} and k_{ZN}) and the ZN transition probability (black line).

An implicit assumption in this treatment of hindered rotations is that rotamer interconversion is fast on the reaction timescale. However, conformational analysis of the trajectories in Fig. 9 shows that while internal rotations are present, they are not fast. For this simplified model we make an approximation to consider only the global S_1 minimum (S_1-B) and a single lowest point on the (3N-7) seam (S_1-TS). Similarity between the frequencies and rotational constants of the conformers suggest that this is an acceptable compromise in this case.

4.3.3 Correcting the NA-EGME model with MS-CASPT2 energies

Our NA-EGME model could be improved by the addition of all inter-conformer transition states. However, the need to search for each critical point on a 3N dimensional PES can undermine the simplicity of the approach proposed here. Instead, we can exploit the comparatively low computational cost of the EGME calculations by using energies calculated with a more sophisticated, multireference, electronic structure method at the stationary points. By assuming that the locations of the stationary points optimised with LR-TDDFT give a broadly accurate representation of the PES, the model can be adjusted by using MS(4)-CASPT2(10,8)/6-31G* energies (with LR-TDDFT frequencies and rotational constants) to calculate the population profile of HPALD over time. Results of this scan are shown in Fig. 12. New parameters are used in the ZN equations, based on the fitting of diabats to new MS-CASPT2 energies calculated across the same eigenvector coordinate as in the earlier calculation.

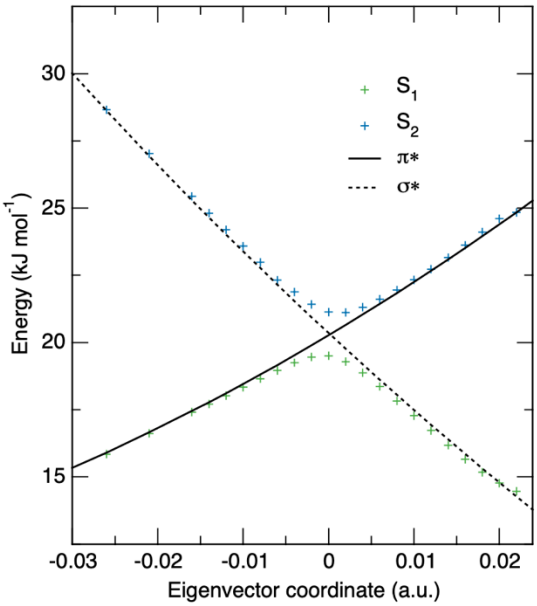

Fig. 12: MS(4)-CASPT2(10,8)/6-31G* scan across the S_1-TS geometry along the eigenvector of the imaginary normal mode, optimised with LR-TDDFT/PBE0/6-31G. Fitted diabatic states used for parameter fitting in the NA-EGME calculation are shown in black

Results of NA-EGME calculations based on MS-CASPT2 energies show that the difference between the nonadiabatic and adiabatic rates is more significant than that produced using TDDFT/PBE0 energies. The adiabatic lifetime of HPALD is $\tau_{\text{A-EGME}}$ = 0.44 ps whereas the nonadiabatic lifetime, $\tau_{\text{NA-EGME}}$ = 30 ps, is 70 times slower. Nonadiabatic coupling between the states is weaker increasing the likelihood of transition to the S_2 state illustrating the sensitivity of the coupling strength to the selected electronic structure method. To improve the quality of the model, accurate multireference methods – often too expensive for on-the-fly excited state dynamics – must be used and we showed in this section how they can be built in to the EGME approach.

5 Discussion

The most direct comparison between the two approaches can be seen in the models that isolate conformer C. Fig. 8 demonstrates the remarkable similarity between the results of trajectory-based methods and EGME: the NA-MD photodissociation lifetime $\tau_{NA\text{-}MD}$ = 1.9 ps is comparable to the NA-EGME lifetime $\tau_{NA\text{-}EGME}$ = 2.7 ps. The impact of nonadiabatic effects on the photodissociation rate is stronger in the EGME results: the calculated adiabatic lifetimes are $\tau_{A\text{-}EGME}$ = 0.5 ps and $\tau_{A\text{-}MD}$ = 1.29 ps. A direct comparison between the decay rates in the extended models that include all conformers can be seen in Fig. 13. Nonadiabatic EGME and NA-MD methods returned lifetimes differing by less than factor of 3: $\tau_{NA\text{-}EGME}$ = 1.7 ps and $\tau_{NA\text{-}MD}$ = 4.6 ps. That these results match to within an order of magnitude is remarkable given the stark differences between the two approaches. For the adiabatic simulations the comparison is made with the slow component of the fitted decay, with $\tau_{A\text{-}EGME}$ = 0.31 ps and $\tau_{A\text{-}MD}$ = 2.4 ps, out by less than a factor of 8. Trajectory surface hopping simulations indicate that a diabatic trapping mechanism is responsible for this deceleration as it causes the nuclear wavepacket to be trapped in a bound diabatic state, preventing direct dissociation. To quantify the impact of nonadiabatic effects at the seam, we compare the ratios of the nonadiabatic/adiabatic lifetimes for both the dynamical and the master equation approaches. We note that Plasser *et al.*[76] showed, in the context of surface hopping and Landau-Zener probabilities, that the difference between the adiabatic and nonadiabatic rates in diabatic trapping processes can be related to the electronic transmission coefficient. This value is 1.9 for the trajectory methods, and 5.5 for the kinetic model. The difference may arise in part from the assumption within the EGME model that allows for only a single seam crossing. Formulations of LZ transition probability that allow for multiple recrossing of the seam have been developed, notably by Delos and Nikitin[77, 78] and could be applied to this method in future work. Another fundamental difference is that EGME is a statistical method which assumes that the system is ergodic - i.e. energy has no preference for residing in a specific mode and can be instantaneously exchanged with all of the available modes in a particular molecule. The accuracy of the ergodicity assumption typically applies to timescales longer than 4 ps. For any dynamical approach at short timescales (including excited-state dynamics), the energy is likely to be distributed in a non-Boltzmann way due to the out-of-equilibrium nature of the dynamics following photoexcitation, and the fact that the timescale for energy redistribution amongst intramolecular modes is finite. Unlike a dynamical approach in which excited-state trajectories can explore different regions of the intersection space, the EGME is ignorant of the broader PES topology, given that the crossing can only occur at the TS along the defined one-dimensional coordinate. We finally note that nonadiabatic tunnelling effects are built-in to the Zhu-Nakamura formulas.

It is also important to highlight that the excited-state dynamics performed here assume the formation of a nuclear wavepacket upon light absorption. Such initial condition corresponds to a scenario where the molecule is photoexcited by an ultrashort laser pulse, rather than continuous irradiation with sunlight as it would happen under atmospheric conditions. The question of selecting proper initial conditions for the excited-state dynamics of atmospheric molecules is discussed further in Suchan *et al.*.[79] A protocol aiming at simulating sunlight absorption processes was also recently proposed.[80] In the context of this work, this assumption does not affect the comparison between the EGME models and the dynamics, but does limit the claims we can make about the atmospheric implications of our results.

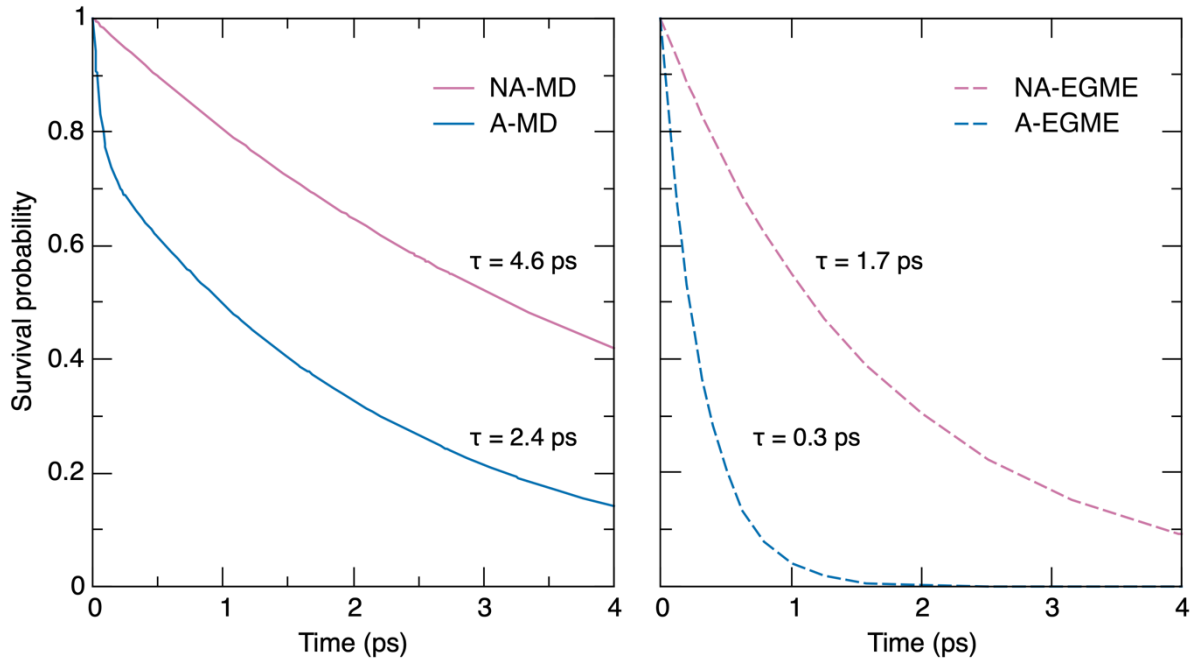

Fig. 13: Side-by-side comparison of the two models used to calculate the dissociation rate for C_6-HPALD. The fit to the population decay is presented for both NA-MD and AIMS.

In this paper we aimed to validate a nonadiabatic EGME model against NA-MD by calculating the rate of OH loss in C_6-HPALD, which has been experimentally investigated by Wolfe *et al.*.[41] We highlight the approximations made in the construction of the master equation model and outline how this model can be improved. Many features of the C_6-HPALD dissociation process seem to justify these approximations. This includes the picosecond timescale of photodissociation; ease of energy exchange between the many modes of HPALD; the (3N-7) geometry of the seam which makes the 1-D seam crossing model appropriate. Of course, the exploratory value of running dynamics simulations cannot be superseded by a model that requires existing knowledge of important stationary points. Without performing the NA-MD calculations the diabatic trapping mechanism would not have been identified. Nonadiabatic transitions are ultimately caused by nuclear motion and so atomistic simulations are necessary for an accurate description of wavepacket dynamics. However, when nonadiabatic transitions between excited states occur on a slow timescale we are limited by the computational cost of running long trajectories and using the NA-EGME model allows us to refine the energies of the critical points whilst reproducing the overall impact of diabatic trapping on the photodissociation rate. The NA-MD calculations are without any doubts more computationally expensive than the NA-EGME approach and would scale less favourably with the number of nuclear degrees of freedom. In instances of slow photodynamic reactions with known mechanisms, alternative models might be explored before choosing to run trajectory dynamics.

The workflow to perform a nonadiabatic EGME analysis on this type of crossing can then be summarised as follows.

1. Locate and characterise the critical points on the excited state PES. These include the bound minima near the Franck-Condon region, the conical intersections, and the adjacent transition states.
2. Identify the normal mode at the crossing point that corresponds to the exciton moving from one chromophore to the other.

3. Perform a scan across this normal mode and fit the shape of the crossing point to a 1-dimensional analytical model.
4. Construct an EGME model of the seam crossing, using the fitting parameters obtained in step 3 for ZN transition probabilities. This utility is currently implemented in MESMER.

These findings describe a type of crossing between adiabatic surfaces that is intermediate to the traditional representation of a two-cone type conical intersection (Fig. 14, left panel) and a fully degenerate seam one might see in the context of intersystem crossing (Fig. 14, right panel). The protocol described here is applicable when calculating rates for this type of trivially unavoided crossing i.e. when collapsing the reaction coordinate to a single dimension is appropriate. These coordinates could be identified through principal component analysis of trajectory dynamics.

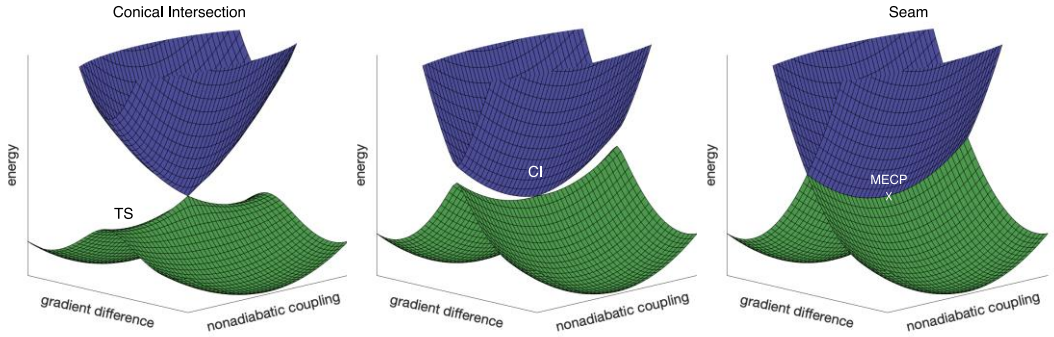

Fig. 14: Types of crossings between adiabatic states, the geometry of the intersection is determined by the extent of the nonadiabatic coupling between states. Central panel represents a model topology like that of the nπ*/n'σ* crossing in C_6-HPALD where the CI is only a single point on an extended seam and so becomes less important in the overall description of the nonadiabatic transition.

6. Conclusions

We directly compared the performance of NA-MD to that of a nonadiabatic EGME model by conducting two side-by-side studies of C_6-HPALD photodissociation. Both methods establish that the nonadiabatic coupling at the extended seam is significant and reduces the rate of OH loss. The lifetimes of C_6-HPALD based on these fundamentally different models indicate that a reduced dimensionality NA-EGME treatment for avoided crossings can reproduce results of dynamics to within an order of magnitude. Further work is needed to investigate the rate of intra-vibrational relaxation between all modes, so as to determine the exact limits of the regime where this kind of protocol can be applied. Similarity between the dynamic and EGME results also raises the question of timescale, since intra-vibrational relaxation must be fast to satisfy the key assumption of RRKM theory. It is unclear whether this is satisfied in this case, and so merits further work to investigate the energy redistribution between modes prior to the dissociation. Some purely dynamical features such as loss of HO_2 could not be included in an EGME treatment, and merit further exploration to determine the significance of HO_2 loss to the atmospheric mechanism. Alongside the significant improvement in computational cost we highlight that approaching this photodissociation mechanism from both the kinetic and the dynamic perspective offers insights into different aspects of the dissociative process.

Supporting Information

The SI contains the optimised ground state geometries of all C_6-HPALD conformers; their energies and Boltzmann weights; a set of electronic structure benchmarks for its exited states; the photoabsorption cross-section; optimised geometries on the S_1 state; energies, frequencies,

and rotational constants of critical points on the S_1 state; branching space vectors of the MECI; plot of peroxide bond lengths over the course of the trajectory; fits of the MD decay rates; discussion of time step size for MD; parameters of the diabatic crossings in 1-D for the LR-TDDFT and MS-CASPT2 TS; sensitivity tests for the EGME model; hindered rotor corrections for the EGME model; full set of Zhu-Nakamura equations; MESMER input files.

Acknowledgements

D.R.G. acknowledges funding from the Royal Society as a University Research Fellow. R.J.S. is supported by EPSRC Programme Grant No. EP/P021123/1. D.S. acknowledges PhD studentship support from the EPSRC Centre for Doctoral Training in Theory and Modelling in Chemical Sciences (EP/L015722/1). This project has received funding from the European Research Council (ERC) under the European Union's Horizon 2020 research and innovation programme (Grant Agreements 803718 and 701355 – Projects SINDAM and NAMDIA). The authors thank Todd Martínez for useful discussions at various stages of this project.

References

1. Lee, M. K.; Coker, D. F., Modeling electronic-nuclear interactions for excitation energy transfer processes in light-harvesting complexes. *J. Phys. Chem. Lett.* **2016,** *7*, 3171 - 3178.
2. Sisto, A.; Stross, C.; van der Kamp, M. W.; O'Connor, M.; McIntosh-Smith, S.; Johnson, G. T.; Hohenstein, E. G.; Manby, F. R.; Glowaki, D. R.; Martínez, T. J., Atomistic non-adiabatic dynamics of the LH2 complex with a GPU-accelerated ab initio exciton model. *Phys. Chem. Chem. Phys.* **2017,** *19*, 14924-14936.
3. Hayes, D.; Griffin, G. B.; Engel, G. S., Engineering coherence among excited states in synthetic heterodimer systems. *Science* **2013,** *340*, 1431-1434.
4. Sisto, A.; Glowacki, D. R.; Martínez, T. J., Ab initio nonadiabatic dynamics of multichromophore complexes: A scalable graphical-processing-unit-accelerated exciton framework. *Acc. Chem. Res.* **2014,** *47*, 2857-2866.
5. Shim, S.; Rebentrost, P.; Valleau, S.; Aspuru-Guzik, A., Atomistic study of the long-lived quantum coherences in the Fenna-Matthews-Olson complex. *Biophys. J.* **2012,** *102*, 649-660.
6. Landau, L. D., A theory of energy transfer II. *Phys. Z. Sowjetunion* **1932,** *2*.
7. Zener, C., Non-adiabatic crossing of energy levels. *Proc. R. Soc. Lond.* **1932,** *137*.
8. Stückelberg, E. C. G., Theory of inelastic collisions between atoms. *Helv. Phys. Acta* **1932,** *5*.
9. Nakamura, H., Semiclassical treatment of nonadiabatic transitions: Multilevel curve crossing and nonadiabatic tunneling problems. *J. Chem. Phys.* **1987,** *87*, 4031-4041.
10. Zhu, C.; Nakamura, H., Theory of nonadiabatic transition for general two-state curve crossing problems. I. Nonadiabatic tunneling case. *J. Chem. Phys.* **1994,** *101*, 10630-10647.
11. Zhu, C.; Nakamura, H., The two-state linear curve crossing problems revisited. II. Analytical approximations for the Stokes constant and scattering matrix: The Landau-Zener case. *J. Chem. Phys.* **1992,** *97*, 8497-8514.
12. Zhu, C.; Nakamura, H., The two-state linear curve crossing problems revisited. I. Analysis of Stokes phenomenon and expressions for scattering matrices. *J. Chem. Phys.* **1992,** *97*, 1892-1904.
13. Zhu, C.; Nakamura, H., The two-state linear curve crossing problems revisited. III. Analytical approximations for Stokes constant and scattering matrix: Nonadiabatic tunneling case. *J. Chem. Phys.* **1993,** *98*, 6208-6222.

14. Zhu, C.; Nakamura, H., Theory of nonadiabatic transition for general two-state curve crossing problems. II. Landau-Zener case. *J. Chem. Phys.* **1995,** *102*, 7448-7461.
15. Zhu, C.; Nakamura, H., Two-state linear curve crossing problems revisited. IV. The best analytical formulas for scattering matrices. *J. Chem. Phys.* **1994,** *101*, 4855-4866.
16. Tully, J. C., Molecular dynamics with electronic transitions. *J. Chem. Phys.* **1990,** *93*.
17. Horenko, I.; Salzmann, C.; Schmidt, B.; Schütte, C., Quantum-classical Liouville approach to molecular dynamics: Surface hopping Gaussian phase-space packets. *J. Chem. Phys.* **2002,** *117*, 11075.
18. Francés-Monerris, A.; Carmona-García, J.; Acuña, A. U.; Dávalos, J. Z.; Cuevas, C. A.; Kinnison, D. E.; Francisco, J. S.; Saiz-Lopez, A.; Roca-Sanjuán, D., Photodissociation mechanisms of major mercury(II) species in the atmospheric chemical cycle of mercury. *Angew. Chem. Int. Ed.* **2020,** *59*, 7605 –7610
19. Rodrigues, G. P.; Ventura, E.; Andrade Do Monte, S.; Barbatti, M., Photochemical deactivation process of HCFC-133a ($C_2H_2F_3Cl$): A nonadiabatic dynamics study. *J. Phys. Chem. A* **2014,** *118*, 12041 - 12049.
20. Prlj, A.; Ibele, L. M.; Marsili, E.; Curchod, B. F. E., On the theoretical determination of photolysis properties for atmospheric volatile organic compounds. *J. Phys. Chem. Lett.* **2020,** *11*, 5418-5425.
21. Shemesh, D.; Gerber, R. B., Femtosecond timescale deactivation of electronically excited peroxides at ice surfaces. *Mol. Phys.* **2012,** *110*, 605 - 617.
22. Westermayr, J.; Gastegger, M.; Menger, F. S. J. M.; Mai, S.; Gonzalez, L.; Marquetand, P., Machine learning enables long time scale molecular photodynamics simulations. *Chem. Sci.* **2019,** *10*, 8100-8107.
23. Blitz, M. A.; Salter, R. J.; Heard, D. E.; Seakins, P. W., An experimental and master equation study of the kinetics of OH/OD + SO_2: The limiting high-pressure rate coefficients. *J. Phys. Chem. A.* **2017,** *121*, 3184-3191.
24. Goldman, L. M.; Glowacki, D. R.; Carpenter, B. K., Nonstatistical dynamics in unlikely places: [1,5] hydrogen migration in chemically activated cyclopentadiene. *J. Am. Chem. Soc.* **2011,** *133*, 5312-5318.
25. Glowacki, D. R.; Liang, C. H.; Marsden, S.; Harvey, J. N.; Pilling, M. J., Alkene hydroboration: Hot intermediates that react while they are cooling. *J. Am. Chem. Soc.* **2010,** *132*, 13621-13623.
26. Glowacki, D. R.; Rodgers, W. J.; Shannon, R.; Robertson, S. H.; Harvey, J. N., Reaction and relaxation at surface hotspots: Using molecular dynamics and the energy-grained master equation to describe diamond etching. *Philos. Trans. R. Soc. A* **2017,** *375*.
27. Bonhommeau, D.; Truhlar, D. G., Mixed quantum/classical investigation of the photodissociation of NH_3(Ã) and a practical method for maintaining zero-point energy in classical trajectories. *J. Chem. Phys.* **2008,** *129*, 014302.
28. Miller, W. H., Tunneling corrections to unimolecular rate constants, with application to formaldehyde. *J. Am. Chem. Soc.* **1979,** *101*, 6810-6814.
29. Garrett, B. C.; Truhlar, D. G., Semiclassical tunneling calculations. *J. Phys. Chem.* **1979,** *83*, 2921-2926.
30. Lorquet, J. C.; Leyh-Nihant, B., Nonadiabatic unimolecular reactions. 1. A statistical formulation for the rate constants. *J. Phys. Chem.* **1988,** *92*, 4778-4783.
31. Hammes-Schiffer, S.; Tully, J. C., Nonadiabatic transition state theory and multiple potential energy surface molecular dynamics of infrequent events. *J. Chem. Phys.* **1995,** *103*, 8528-8537.
32. Lykhin, A. O.; Kaliakin, D. S.; dePolo, G. E.; Kuzubov, A. A.; Varganov, S. A., Nonadiabatic transition state theory: Application to intersystem crossings in the active sites of metal-sulfur proteins. *Int. J. Quantum Chem.* **2016,** *116*, 750-761.

33. Harvey, J. N.; Aschi, M., Modelling spin-forbidden reactions: Recombination of carbon monoxide with iron tetracarbonyl. *Faraday Discuss.* **2003,** *124*, 129-143.
34. Harvey, J. N., Understanding the kinetics of spin-forbidden chemical reactions. *Phys. Chem. Chem. Phys.* **2006,** *9*, 331-343.
35. Zaari, R. R.; Varganov, S. A., Nonadiabatic transition state theory and trajectory surface hopping dynamics: Intersystem crossing between $^3B_1$ and $^1A_1$ states of SiH_2. *J. Phys. Chem. A* **2015,** *119*, 1332-1338.
36. Lykhin, A. O.; Varganov, S. A., Intersystem crossing in tunneling regime: $T_1 \rightarrow S_0$ relaxation in thiophosgene. *Phys. Chem. Chem. Phys.* **2020,** *22*, 5500-5508.
37. Maiti, B.; Schatz, G. C.; Lendvay, G., Importance of intersystem crossing in the $S(^3P, ^1D) + H_2 \rightarrow SH + H$ reaction. *J. Phys. Chem. A* **2004,** *108*, 8772-8781.
38. Granucci, G.; Persico, M.; Spighi, G., Surface hopping trajectory simulations with spin-orbit and dynamical couplings. *J. Chem. Phys.* **2012,** *137*.
39. Richter, M.; Marquetand, P.; González-Vázquez, J.; Sola, I.; González, L., SHARC – ab initio molecular dynamics with surface hopping in the adiabatic representation including arbitrary couplings. *J. Chem. Theory Comput.* **2011,** *7*, 1253-1258.
40. Mai, S.; Marquetand, P.; Gonzalez, L., A general method to describe intersystem crossing dynamics in trajectory surface hopping. *Int. J. Quantum Chem.* **2015,** *115*, 1215-1231.
41. Wolfe, G. D.; Crounse, J. D.; Parrish, J. D.; St. Clair, J. M.; Beaver, M. R.; Paulot, F.; Yoon, T. P.; Wennberg, P. O.; Keutsch, F. N., Photolysis, OH reactivity and ozone reactivity of a proxy for isoprene-derived hydroperoxyenals (HPALDs). *Phys. Chem. Chem. Phys.* **2012,** *14*, 7276-7286.
42. Peeters, J.; Müller, J.-F.; Stavrakou, T.; Nguyen, V. S., Hydroxyl radical recycling in isoprene oxidation driven by hydrogen bonding and hydrogen tunneling: The upgraded LIM1 mechanism. *J. Phys. Chem. A* **2014,** *118*, 8625-8643.
43. Peeters, J.; Muller, J. F., HO_x radical regeneration in isoprene oxidation via peroxy radical isomerisations. II: Experimental evidence and global impact. *Phys. Chem. Chem. Phys.* **2010,** *12*, 14227-14235.
44. Peeters, J.; Nguyen, T. L.; Vereecken, L., HO_x radical regeneration in the oxidation of isoprene. *Phys. Chem. Chem. Phys.* **2009,** *11*, 5935-5939.
45. Taraborrelli, D.; Lawrence, M. G.; Crowley, J. N.; Dillon, T. J.; Gromov, S.; Groß, C. B. M.; Vereecken, L.; Lelieveld, J., Hydroxyl radical buffered by isoprene oxidation over tropical forests. *Nature Geosci.* **2012,** *5*, 190-193.
46. Lelieveld, J.; Butler, T. M.; Crowley, J. N.; Dillon, T. J.; Fischer, H.; Ganzeveld, L.; Harder, H.; Lawrence, M. G.; Martinez, M.; Taraborrelli, D., et al., Atmospheric oxidation capacity sustained by a tropical forest. *Nature* **2008,** *452*, 737-740.
47. Hansen, R. F.; Lewis, T. R.; Graham, L.; Whalley, L. K.; Seakins, P. W.; Heard, D. E.; Blitz, M. A., OH production from the photolysis of isoprene-derived peroxy radicals: Cross-sections, quantum yields and atmospheric implications. *Phys. Chem. Chem. Phys.* **2017,** *19*, 2332-2345.
48. Glowacki, D. R.; Lockhart, J.; Blitz, M. A.; Klippenstein, S. J.; Pilling, M. J.; Robertson, S. H.; Seakins, P. W., Interception of excited vibrational quantum states by O_2 in atmospheric association reactions. *Science* **2012,** *337*, 1066-1069.
49. Plane, J. M. C.; Whalley, C. L.; Frances-Soriano, L.; Goddard, A.; Harvey, J. N.; Glowacki, D. R.; Viggiano, A. A., $O_2(a^1\Delta_g)$ + Mg, Fe, and Ca: Experimental kinetics and formulation of a weak collision, multiwell master equation with spin-hopping. *J. Chem. Phys.* **2012,** *137*, 014310.
50. Vereecken, L.; Glowacki, D. R.; Pilling, M. J., Theoretical chemical kinetics in tropospheric chemistry: Methodologies and applications. *Chem. Rev.* **2015,** *115*, 4063-4114.

51. Nakamura, H., Dynamics of nonadiabatic chemical reactions. *J. Phys. Chem. A* **2006,** *110*, 10929-10946.
52. Glowacki, D. R.; Lightfoot, R.; Harvey, J. N., Non-equilibrium phenomena and molecular reaction dynamics: Mode space, energy space and conformer space. *Mol. Phys.* **2013,** *111*, 631-640.
53. Glowacki, D. R.; Liang, C.-H.; Morley, C.; Pilling, M. J.; Robertson, S. H., MESMER: An open-source master equation solver for multi-energy well reactions. *J. Phys. Chem. A* **2012,** *116*, 9545-9560.
54. Tozer, D. J., Relationship between long-range charge-transfer excitation energy error and integer discontinuity in Kohn–Sham theory. *J. Chem. Phys.* **2003,** *119*.
55. Levine, B. G.; Ko, C.; Quenneville, J.; Martinez, T. J., Conical intersections and double excitations in time-dependent density functional theory. *Mol. Phys.* **2006,** *104*.
56. Agostini, F.; Curchod, B. F. E.; Vuilleumier, R.; Tavernelli, I.; Gross, E. K. U., TDDFT and quantum-classical dynamics: a universal tool describing the dynamics of matter. In *Handbook of Materials Modeling: Methods: Theory and Modeling*, Andreoni, W.; Yip, S., Eds. Springer International Publishing: Cham, 2020; pp 75-121.
57. Curchod, B. F. E.; Rothlisberger, U.; Tavernelli, I., Trajectory-based nonadiabatic dynamics with time-dependent density functional theory. *Chem. Phys. Chem. Rev.* **2013,** *14*, 1314-1340.
58. Frisch, M. J.; Trucks, G. W.; Schlegel, H. B.; Scuseria, G. E.; Robb, M. A.; Cheeseman, J. R.; Scalmani, G.; Barone, V.; Petersson, G. A.; Nakatsuji, H., et al. *Gaussian 16, Revision C.01*, Gaussian, Inc.: Wallingford CT, 2016.
59. Werner, H.-J.; Knowles, P. J.; Knizia, G.; Manby, F. R.; Schütz, M.; Celani, P.; Györffy, W.; Kats, D.; Korona, T.; Lindh, R., et al. *MOLPRO, version 2019.2, a package of ab initio programs*, 2019.
60. Galván, I. F.; Vacher, M.; Alavi, A.; Angeli, C.; Aquilante, F.; Autschbach, J.; Bao, J. J.; Bokarev, S. I.; Bogdanov, N. A.; Carlson, R. K., et al., OpenMolcas: From source code to insight. *J. Chem. Theory Comput.* **2019,** *15*, 5925-5964.
61. Harvey, J. N.; Aschi, M.; Schwarz, H.; Koch, W., The singlet and triplet states of phenyl cation. A hybrid approach for locating minimum energy crossing points between non-interacting potential energy surfaces. *Theo. Chem. Acc.* **1997,** *99*, 95-99.
62. Crespo-Otero, R.; Barbatti, M., Spectrum simulation and decomposition with nuclear ensemble: Formal derivation and application to benzene, furan and 2-phenylfuran. *Theo. Chem. Acc.* **2012,** *131*, 1-14.
63. Barbatti, M.; Granucci, G.; Persico, M.; Ruckenbauer, M.; Vazdar, M.; Eckert-Maksić, M.; Lischka, H., The on-the-fly surface-hopping program system Newton-X: Application to *ab initio* simulation of the nonadiabatic photodynamics of benchmark systems. *J. Photochem. Photobiol. A* **2007,** *190*, 228–240.
64. Frisch, M. J.; Trucks, G. W.; Schlegel, H. B.; Scuseria, G. E.; Robb, M. A.; Cheeseman, J. R.; Scalmani, G.; Barone, V.; Mennucci, B.; Petersson, G. A., et al. *Gaussian 09, Revision A.02*, Gaussian, Inc.: Wallingford CT, 2016.
65. Granucci, G.; Persico, M., Critical appraisal of the fewest switches algorithm for surface hopping. *J. Chem. Phys.* **2007,** *126*, 134114.
66. Pittner, J.; Lischka, H.; Barbatti, M., Optimization of mixed quantum-classical dynamics: Time-derivative coupling terms and selected couplings. *Chem. Phys.* **2009,** *356*, 147-152.
67. Holbrook, K. A.; Pilling, M. J.; Robertson, S. H., *Unimolecular Reactions*. John Wiley & Sons: New York, 1996; p 417.

68. Lasorne, B.; Bacchus-Montabonel, M.-C.; Vaeck, N.; Desouter-Lecomte, M., Nonadiabatic interactions in wave packet dynamics of the bromoacetyl chloride photodissociation. *J. Chem. Phys.* **2004,** *120*, 1271–1278.
69. Martínez, T. J., Ab initio molecular dynamics around a conical intersection: Li(2p) + H_2. *Chem. Phys. Lett.* **1997,** *272*, 139-147.
70. Blancafort, L.; Hunt, P.; Robb, M. A., Intramolecular electron transfer in bis(methylene) adamantyl radical cation: A case study of diabatic trapping. *J. Am. Chem. Soc.* **2005,** *127*, 3391-3399.
71. Baasandorj, M.; Papanastasiou, D. K.; Talukdar, R. K.; Hasson, A. S.; Burkholder, J. B., $(CH_3)_3COOH$ (tert-butyl hydroperoxide): OH reaction rate coefficients between 206 and 375 K and the OH photolysis quantum yield at 248 nm. *Phys. Chem. Chem. Phys.* **2010,** *12*, 12101-12111.
72. Ibele, L. M.; Curchod, B. F. E., A molecular perspective on Tully models for nonadiabatic dynamics. *Phys. Chem. Chem. Phys.* **2020,** *22*, 15183-15196.
73. Glowacki, D. R.; Reed, S. K.; Pilling, M. J.; Shalashilin, D. V.; Martínez-Núñez, E., Classical, quantum and statistical simulations of vibrationally excited $HOSO_2$: IVR, dissociation, and implications for OH + SO_2 kinetics at high pressures. *Phys. Chem. Chem. Phys.* **2009,** *11*, 963—974.
74. Zheng, J.; Truhlar, D. G., Multi-path variational transition state theory for chemical reaction rates of complex polyatomic species: Ethanol + OH reactions. *Faraday Discuss.* **2012,** *157*, 59.
75. Sharma, S.; Raman, S.; Green, W. H., Intramolecular hydrogen migration in alkylperoxy and hydroperoxyalkylperoxy radicals: Accurate treatment of hindered rotors. *J. Phys. Chem. A* **2010,** *114*, 5689–5701.
76. Plasser, F.; Granucci, G.; Pittner, J.; Barbatti, M.; Persico, M.; Lischka, H., Surface hopping dynamics using a locally diabatic formalism: Charge transfer in the ethylene dimer cation and excited state dynamics in the 2-pyridone dimer. *J. Chem. Phys.* **2012,** *137*, 22A514.
77. Delos, J. B., On the reactions of N_2 with O. *J. Chem. Phys.* **1973,** *59*, 2365-2369.
78. Nikitin, E. E., Nonadiabatic transitions: What we learned from old masters and how much we owe them. *Annu. Rev. Phys. Chem.* **1999,** *50*, 1-21.
79. Suchan, J.; Hollas, D.; Curchod, B. F. E.; Slavíček, P., On the importance of initial conditions for excited-state dynamics. *Faraday Discuss.* **2018,** *212*, 307-330.
80. Barbatti, M., Simulation of excitation by sunlight in mixed quantum-classical dynamics. *J. Chem. Theo. Comput.* **2020,** *16*, 4849-4856.

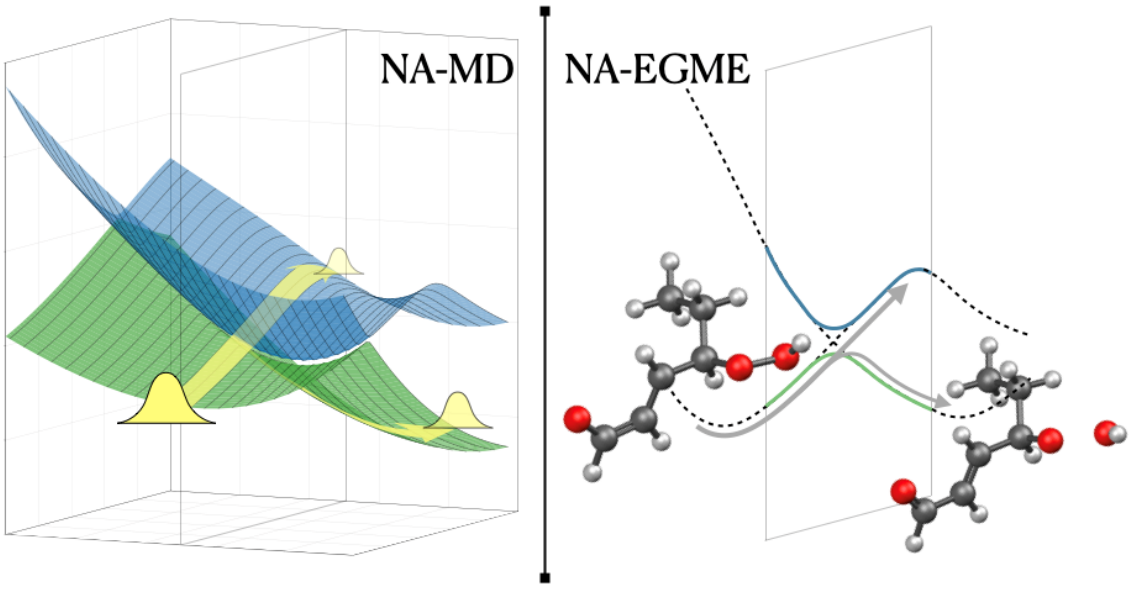
NA-MD
NA-EGME